Full length article

Orientation dependent pinning of (sub)grains by dispersoids during recovery and recrystallization in an Al–Mn alloy

Håkon W. Ånes [a], Antonius T.J. van Helvoort [b], Knut Marthinsen [a,*]

[a] Department of Materials Science and Engineering, Norwegian University of Science and Technology, 7491, Trondheim, Norway
[b] Department of Physics, Norwegian University of Science and Technology, 7491, Trondheim, Norway

ARTICLE INFO

ABSTRACT

The recrystallized grain size and texture in alloys can be controlled via the microchemistry state during thermomechanical processing. The influence of concurrent precipitation on recovery and recrystallization is here analyzed by directly correlating (sub)grains of P, CubeND and Cube orientation with second-phase particles in a cold-rolled and non-isothermally annealed Al–Mn alloy. The recrystallized state is dominated by coarse elongated grains with a strong P, weaker CubeND and even weaker Cube texture. The correlated data enables orientation dependent quantification of density and size of dispersoids on sub-boundaries and of subgrains in the deformation zones around large constituent particles. A new modified expression for the Smith–Zener drag from dispersoids on sub-boundaries is derived and used. The results show that drag on (sub)grain boundaries from dispersoids is orientation dependent, with Cube subgrains experiencing the highest drag after recovery and partial recrystallization. The often-observed size advantage of Cube subgrains is not realized due to increased drag, thereby promoting particle-stimulated nucleation (PSN). Relatively fewer and larger dispersoids in deformation zones around large particles give a reduced drag on PSN nuclei, further strengthening PSN. Observations substantiating stronger P texture compared to CubeND texture are higher frequency of P subgrains and faster growth of these subgrains. The applied methodology enables a better understanding of the mechanisms behind the orientation dependent nucleation and growth behavior during recovery and recrystallization with strong concurrent precipitation in Al–Mn alloys. In particular, the methodology gives new insights into the strong P and CubeND textures compared to the Cube texture.

1. Introduction

Al–Mn AA3xxx alloys are widely used in a broad range of products including beverage cans, automotive heat exchangers and packaging, where tailoring the grain size and texture during thermomechanical processing is key to achieve desired properties [1]. Second-phase particles usually form in these alloys during casting, while a high concentration of alloying elements might remain in solid solution and precipitate during subsequent heat treatments. During back annealing after hot and cold rolling, large constituent particles ($\gtrsim 1 \mu$m) may promote recrystallization by particle-stimulated nucleation (PSN) [2,3], while closely spaced fine dispersoids (sub-micron) may retard or even inhibit the transformation by pinning (sub)grain boundaries via Smith–Zener pinning [4–6]. When precipitated prior to or during recovery and recrystallization, the latter termed 'concurrent precipitation', these dispersoids often result in slow recrystallization kinetics and coarse elongated grains [7–12]. The final recrystallization texture after strong PSN is usually weak, but with concurrent precipitation, unusually sharp

P (typically $\{011\}\langle\bar{5}66\rangle$) and ND-rotated cube ($\{001\}\langle310\rangle$, CubeND) textures have been observed [9–12]. This strong P texture in particular is generally attributed to P (sub)grain boundaries experiencing a reduced Smith–Zener drag compared to those of CubeND and Cube ($\{001\}\langle100\rangle$) (sub)grains. This assumption is based on extensive but indirect observations, where typically the microchemistry, in terms of number density and particle size, and the microstructure, in terms of grain size and texture, are analyzed separately.

Recently, the present authors demonstrated an experimental procedure to directly correlate (sub)grains and particles in a recovered Al–Mn alloy [13]. The procedure enables correlated analysis of subgrains in deformation zones surrounding constituent particles and dispersoids located at (sub)grain boundaries. In this work, this procedure is used to study the effect of large constituent particles and fine dispersoid particles on (sub)grains from the as deformed state to partial recrystallization with concurrent precipitation in a cold-rolled Al–Mn alloy. The investigated alloy is the same as the one studied by Huang et al. [10,12]

---

* Corresponding author.
E-mail address: knut.marthinsen@ntnu.no (K. Marthinsen).

(termed 'C1' by them), in which they observed the unusually sharp P texture upon non-isothermal annealing with significant concurrent precipitation. By using the same thermomechanical processing as them from deformation to full recrystallization, the objective of this work is to quantify the orientation dependent effects of particles on (sub)grains during recovery and recrystallization with concurrent precipitation. It is demonstrated that these data can provide insight into the mechanisms behind the strong P and CubeND textures compared to the Cube texture with concurrent precipitation in Al–Mn alloys.

2. Experimental methods

The Al–Mn alloy supplied by Hydro Aluminium is direct-chill cast and has a composition of Al–0.53Fe–0.39Mn–0.152Si wt.%. It is homogenized in an air-circulation furnace from room temperature to 450 °C at a heating rate of 50 °C h^{-1}, held for 4 h and then water quenched. The homogenized material is cold-rolled to a true strain of $\varepsilon = -\ln(h/h_0) = 3$, corresponding to a reduction in thickness h of 95%. The material is finally annealed in an air circulation furnace at a heating rate of 50 °C h^{-1}, with samples retrieved at intervals of 50 °C up to 400 °C.

The recrystallization kinetics are characterized by measuring the electrical conductivity, hardness and macrotexture of the samples including the as deformed material. These measurements are performed on the sample surface spanned by the rolling direction (RD) and the transverse direction (TD). The hardness HV is measured with a *Leica Pros VMHT Vickers* indenter with a load of 1 kg and a dwell time of 15 s, and the hardness per sample is an average of ten measurements with an uncertainty of two standard deviations. The electrical conductivity is measured with a *Foerster Sigmatest 2.069* tester, and the conductivity per sample is an average of 30 measurements with an uncertainty of two standard deviations. The macrotexture is measured with X-ray diffraction (XRD) using a *Siemens Diffractometer D5000* with a copper anode operated at 40 kV and a measurement spot with a diameter of about 2 mm. Samples are prepared for macrotexture measurements by mechanical polishing, etching in *Alubeis* (a mixture of 10%–20% NaOH and sugar) and final etching in 20%–30% HNO$_3$. Four incomplete pole figures {111}, {200}, {220} and {311} of Al, after correction with respect to background intensity and defocusing error, are used to calculate the orientation distribution function (ODF) using *MTEX* v5.8 [14]. Volume fractions, of typical texture components in cold-rolled and recrystallized Al, are then calculated using an orientation spread of 15° from the ideal orientation and an orthorhombic sample symmetry valid for cold-rolled samples. The typical texture components in cold-rolled Al are copper ({112}⟨11$\bar{1}$⟩, C), S ({123}⟨634⟩) and brass ({011}⟨2$\bar{1}$1⟩, B), which make up the β-fiber [5]. The recrystallization texture components of interest in this work are the mentioned Cube, CubeND and P. The total volume fraction can be higher than 100% since the 15° spread leads to overlapping regions in orientation space for some texture components.

SEM measurements are performed on the sample surface spanned by the RD and the normal direction (ND). The sample embedded in epoxy is mechanically polished using diamond paste down to 1 μm grain size, followed by vibration polishing in a *Buehler VibroMet 2* using colloidal silica of 0.05 μm grain size. The final deformed surface layer is removed with ion polishing in a *Hitachi IM-3000* using Ar$^+$ ions accelerated to 3 keV with the sample tilted 60° from the horizontal and rotating. The sample is plasma cleaned with a *Fischione 1020* prior to insertion in the SEM. This sample preparation was chosen because it provides a sample surface sufficiently free of deformation for EBSD analysis, while only a limited number of particles are visibly removed from it.

Particles are detected in backscatter electron (BSE) images with a resolution of about 0.026 μm, acquired in a *Zeiss Ultra 55* FEG SEM operated at 5 kV. A particle detection procedure for the sample at 300 °C is described by the authors in Ref. [13]. In order to achieve

satisfactory quantitative particle detection from BSE images with varying intensity distributions, some modifications to this procedure are required. To obtain comparable intensity distributions, intensities in all images are matched using histogram matching to the intensities in a BSE image obtained at 300 °C. Furthermore, instead of detecting particles via region-based segmentation, large and small particles are detected in two separate images using automatic thresholding. Larger particles are detected in the histogram matched image after applying rolling ball averaging with a ball radius of one pixel, effectively blurring out the small particles. Smaller particles are detected in the image obtained from subtracting the rolling ball averaged image from the histogram matched image, effectively masking out the larger particles. After thresholding, these two images are combined into the final binary particle map, where any incorrectly detected particles are removed as described in Ref. [13]. Image processing is done with *ImageJ* [15].

(Sub)grain orientations and sizes are mapped using electron backscatter diffraction (EBSD) from the same regions of interest (ROIs) as the BSE images. The same SEM as for particle detection is used, but operated at 17 kV with a sample tilt of 70° and a nominal step size of 0.1 μm. EBSD patterns are acquired with a *NORDIF UF-1100* detector with a binning factor of 5, 6 or 8 to pattern resolutions of (96 × 96), (80 × 80) or (60 × 60) pixels, respectively, with acquisition speeds in the range of 70–350 patterns s^{-1}. These acquisition parameters are chosen to provide a sufficient signal-to-noise ratio on the detector within a reasonable acquisition time. Patterns are indexed as Al (space group $Fm\bar{3}m$, $a = 0.404$ nm) by dictionary indexing [16] followed by refinement as implemented in *kikuchipy* v0.6 [17,18], using a dynamical master pattern simulated with *EMsoft* v4.3 [19]. An average projection center (PC) for each dataset is obtained by Hough indexing of (240 × 240) pixel calibration patterns with *PyEBSDIndex* v0.1 [20].

In order to analyze particles and (sub)grains from the same ROI in the same reference frame, the EBSD and particle maps are overlapped via image registration as described in Ref. [13], accounting for the different step sizes and any distortions in the EBSD map. Three multimodal datasets are thus obtained from each condition of interest, covering a total area of 0.020–0.028 mm^2 per condition. Orientations are analyzed with *MTEX* [21] as detailed in Ref. [13]. No averaging or clean-up of orientations is required even in the datasets of the as deformed state, as dictionary indexing is capable of indexing EBSD patterns with a relatively low signal-to-noise ratio [22]. The particle map is used to create a 'dual phase' dataset to distinguish between points with Al and points with particles. Reconstructed (sub)grains are classified by texture component based on the lowest misorientation angle between the (sub)grain mean orientation and the components' ideal orientations within a misorientation angle threshold of 15°. (Sub)grains outside the threshold are considered 'random'. As with the macrotexture measurements, an orthorhombic sample symmetry is assumed when classifying (sub)grains. (Sub)grain sizes D and particle sizes d are given as equivalent circular diameters $0.816 \cdot 2 \cdot \sqrt{A/\pi}$, where A is the (sub)grain or particle area. The prefactor follows from considering that the observed 2D plane cuts 3D particles at random [5]. An example of a small part of a BSE image and the resulting multimodal dataset are shown in Fig. 1(a) and (b) respectively, where particles possibly smaller than the EBSD step size are included in the same dataset as (sub)grains and boundaries. Overviews of all multimodal datasets used in this paper are given in Figs. S1–S4 in the supplementary material. The raw EBSD datasets and BSE images are available from Zenodo [23].

3. Results

3.1. Recrystallization kinetics

The changes in electrical conductivity (EC) and hardness as a function of the non-isothermal annealing temperature are shown in Fig. 2(a) with the rate of change in (b, c). The material starts to recover above
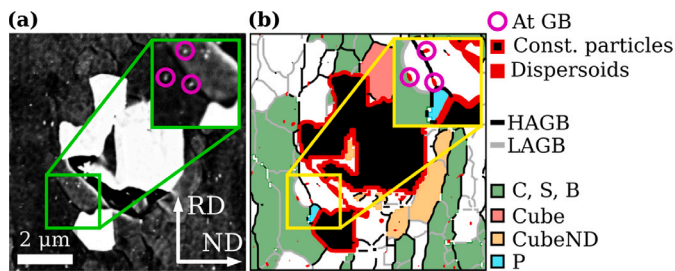
Fig. 1. An example of a small region of a multimodal dataset obtained following a procedure similar to the one reported in Ref. [13], where detected particles in a BSE image (a) are marked in an EBSD map (b) which is corrected for distortions. The multimodal dataset contains (sub)grains classified by texture component, low-angle or high-angle boundaries (LAGB or HAGB) between subgrains, larger constituent particles and smaller dispersoid particles, some of which are located at boundaries as highlighted in the inset.

Fig. 2. Recrystallization kinetics of the cold-rolled and non-isothermally annealed Al–Mn alloy. (a) Electrical conductivity (EC, left) and hardness (right) and their rate of change in (b) and (c), respectively. The temperature intervals for recovery and recrystallization (RX) are highlighted in light and darker gray, respectively. Four conditions selected for detailed analysis of particle and subgrain statistics are highlighted in bold vertical lines. (For interpretation of the references to color in this figure legend, the reader is referred to the web version of this article.)
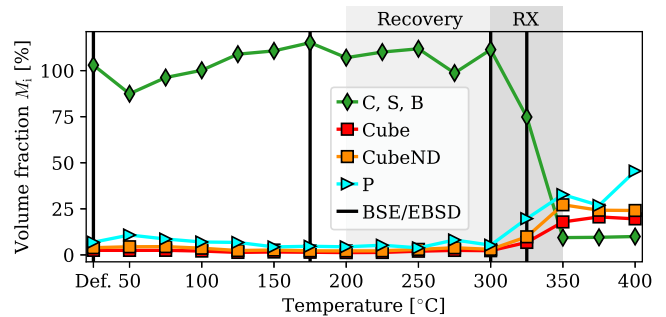
Fig. 3. XRD macrotexture volume fractions M_i per texture component in the cold-rolled and non-isothermally annealed Al–Mn alloy. Volume fractions are given as a function of annealing temperature from the as deformed ('Def.') to after the fully recrystallized state. The temperature intervals for recovery and recrystallization (RX) are highlighted in light and darker gray, respectively. Four conditions selected for detailed analysis of particle and subgrain statistics are highlighted in bold vertical lines. (For interpretation of the references to color in this figure legend, the reader is referred to the web version of this article.)

200 °C and is fully recrystallized above 350 °C, at which point it has a coarse elongated grain structure. BSE imaging and EBSD show no clearly recrystallized grains at 300 °C, but that the material is partly recrystallized at 325 °C. This indicates that recrystallization starts just above 300 °C. The general increase in conductivity with annealing is evidence of precipitation concurrent with recovery and recrystallization, with an increased rate during recovery from 200 °C to 300 °C and an even higher rate during recrystallization from 300 °C to 350 °C. Minimal precipitation is observed after recrystallization has completed. To check the possibility for further precipitation, the conductivity is measured of the material non-isothermally annealed to 400 °C, and then held at that temperature for 10^5 s. The conductivity after this holding time increased by $(1.23 \pm 0.04)\,\text{m}\,\Omega^{-1}\,\text{mm}^{-2}$, i.e. some further precipitation occurred. This shows that what is practically a stop in precipitation after complete recrystallization is temporary, and that further annealing at higher temperatures for longer times is required to continue the precipitation. A similar behavior was observed by Vatne et al. [7] in an AA3103 alloy where precipitation occurred primarily during recrystallization, irrespective of the isothermal annealing temperature. They argued that this indicated that precipitation was not diffusion controlled, but that elements in solid solution precipitated on the moving boundaries of recrystallized grains, a description which fits the precipitation behavior observed here as well.

The XRD macrotexture volume fractions M_i per texture component are plotted as a function of annealing temperature in Fig. 3. As expected for cold-rolled Al, the as deformed microstructure is characterized by a strong β-fiber texture running from the C component over S to B. Upon recrystallization, this deformation texture is superseded by a recrystallization texture dominated by the P, CubeND and Cube components. The ratios of P to CubeND and Cube volume fractions after recrystallization at 400 °C are about 1.9 and 2.3, respectively.

The as deformed state, softening and precipitation behavior and recrystallized grain structure and texture are all comparable to those observed by Huang et al. [10,12] for the same alloy and thermomechanical processing. Their final recrystallization texture was characterized after non-isothermal annealing to 400 °C followed by an additional holding time of 10^5 s at the same temperature. The P texture was reported to be about 4 and 6.7 times stronger than CubeND and Cube, respectively. The relatively stronger P texture reported by them compared to the present strength is assumed to be a result of grain coarsening following primary recrystallization. These comparisons show that recovery and recrystallization in the alloy in this work is similar to that reported by Huang et al.. This allows us to draw from their characterization of the recrystallized material, and instead focus on the causes of the dominating P texture after recovery and recrystallization with significant concurrent precipitation. To that end, four conditions of interest are selected for detailed analysis of particles and (sub)grain statistics, namely the as deformed state and the material
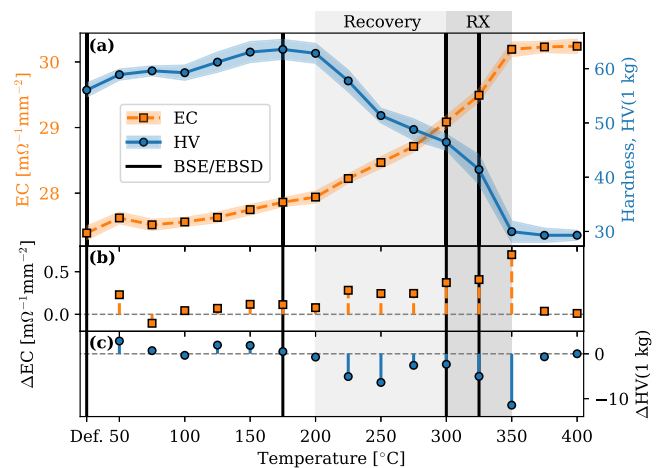
before recovery at 175 °C, after recovery at 300 °C and after partial recrystallization at 325 °C. These conditions are highlighted by bold vertical lines in Figs. 2 and 3.

3.2. Precipitation kinetics

Before correlating particle locations with (sub)grains and (sub)grain boundaries, the precipitation kinetics and subgrain growth from the four analyzed conditions are presented separately. The changes in particle volume fraction f_V as estimated from the surface area fraction, the number of particles per area n_s and the area weighted particle size d_A from the as deformed to the partly recrystallized state are shown in Fig. 4. Values are presented for all particles, constituent particles and dispersoid particles. Particles with sizes d in the range 0.03–0.24 μm are classified as dispersoids based on the approximately bimodal particle size distributions in all conditions (Fig. S5 in the supplementary material). The critical lower diameter of particles considered to be potential nucleation sites for recrystallized grains, i.e. contributing to PSN and in the following labeled 'constituent', after rolling to 95% is about 1 μm [2]. The lower diameter threshold for constituent particles
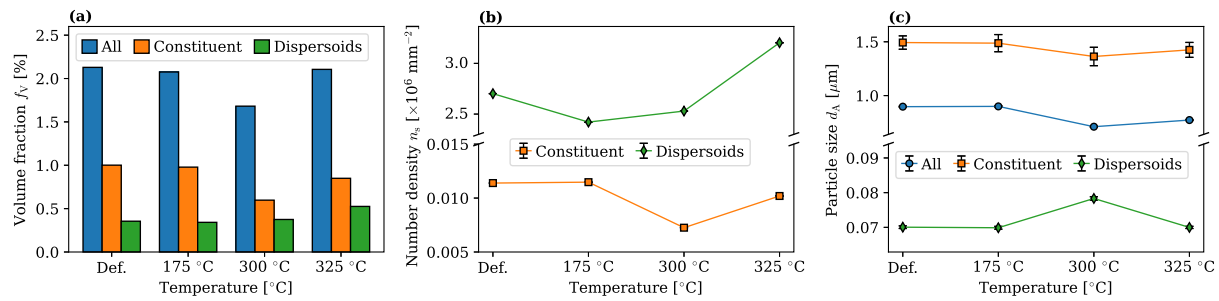
Fig. 4. Precipitation kinetics of the cold-rolled and non-isothermally annealed Al–Mn alloy. (a) Volume fraction f_V, (b) number density n_s with 95% confidence intervals and (c) area weighted particle size d_A with 95% confidence intervals as a function of annealing temperature from the as deformed ('Def.') to the partly recrystallized state for all, constituent and dispersoid particles separately. In (b), the number density of all particles is omitted, and the confidence intervals are so narrow they do not show. Note the broken vertical axes in (b, c).

used here is 0.8 μm due to the stereological considerations mentioned at the end of Section 2. In each condition, the total number of particles, constituent particles and dispersoids ranges from about 68 000 to 118 000, 150 to 300 and 45 000 to 71 000 for the three populations, respectively. The volume fraction f_V of all particles is about 2%, and is approximately the same for all particles and constituent particles in the as deformed and the partly recrystallized state. The drop in f_V at 300 °C seen in Fig. 4 results from fewer detected constituent particles, which is most likely due to their partial inhomogeneous dispersion in the deformed material. The number density n_s and size of constituent particles are approximately constant during recovery and recrystallization (gray ranges in Figs. 2 and 3). The volume fraction of dispersoids increases during recovery and substantially during recrystallization, in line with increases in the rate of change of conductivity in Fig. 2(b). The increase in f_V during recovery results from coarsening of dispersoids, giving an increased average dispersoid size. The substantial increase in f_V during recrystallization results mainly from increased precipitation, as evident from the increased n_s. The increased n_s during recrystallization corresponds to a reduced average dispersoid size.

To assess whether PSN nuclei experience a reduced Smith–Zener drag from dispersoids in the initial stages of recrystallization, the number of dispersoids per area n_s in an area a certain distance from constituent particles, often called the dispersoid-free zone [9,24], relative to n_s elsewhere is calculated. The relative density in the area extending 0.5 μm out from constituent particles is about 95% before recovery and drops to about 80% after partial recrystallization. When extending the area out to 1 μm, there is no clear difference in n_s close to constituent particles and elsewhere. Furthermore, dispersoids in the area out to 0.5 μm have a diameter about 1.5 times greater than dispersoids elsewhere. These results indicate that while the area within 0.5 μm of constituent particles is not free of dispersoids, subgrains in this area experience a reduced Smith–Zener drag upon growth since they encounter fewer and larger dispersoids than subgrains elsewhere.

3.3. Subgrain growth

Changes in subgrain volume fraction F_V, number of subgrains per area N_s and the area weighted subgrain size D_A from the as deformed to the partly recrystallized state are shown in Fig. 5 per texture component and for all other subgrains, labeled 'random' subgrains. In each of the four conditions, the total number of subgrains analyzed ranges from about 60 000 in the as deformed state to about 10 900 in the partly recrystallized state. Recrystallized grains in the partly recrystallized state are excluded from this analysis. A recrystallized grain is classified as having a grain size $D > 4$ μm, a grain orientation spread <1° and with >50% of its boundary having a misorientation angle $\omega > 15°$, which is considered a high angle grain boundary (HAGB). In the as deformed state, there are mostly subgrains of deformation orientations, labeled 'deformation' subgrains, and random subgrains. Both the volume fraction F_V and number density N_s of P subgrains are two and five times

higher than that of CubeND and Cube subgrains, respectively. This indicates that the P texture has a frequency advantage. All subgrains are of a similar size [Fig. 5(c)], except for the deformation subgrains which are much larger. This is due to their location in deformation bands of similar orientations extending in the rolling direction. With annealing, the volume fractions of deformation and random subgrains stay approximately constant, while their number densities decrease after recovery and partial recrystallization. The volume fractions of subgrains of recrystallization orientations, labeled 'recrystallization' subgrains, are all between 0.5%–2% until partial recrystallization. While their volume fractions are comparable at this condition, the number density of P subgrains remains higher than the number densities of CubeND and Cube subgrains. All subgrains apart from deformation subgrains grow in size during recovery and recrystallization. The P and CubeND subgrains are the smallest in the partly recrystallized state.

3.4. Effects of constituent particles on subgrains

Since the particles and subgrains making up the above statistics in Figs. 4 and 5 are acquired within the same regions of interest, they can be combined into multimodal datasets [13]. Each map point in the datasets contains parts of a particle and its size, including those smaller than the EBSD step size, or an Al orientation if there is no particle there. The location and area of effect of larger particles are more challenging to characterize in spatially correlated 2D maps compared to smaller particles. This is because it is possible that a large particle is located beneath or was located above the polished surface, and thus might have affected the (sub)grains on the analyzed surface. Zhang et al. discussed this scenario when they spatially correlated recrystallization nuclei and particles in a multimodal 3D dataset from an Al–Mn alloy cold-rolled and annealed to partial recrystallization [25]. They observed that the fraction of nuclei at clusters or bands of large particles was underestimated from a single 2D slice compared to the fraction from the full 3D dataset. To avoid that this underestimation affects the analysis in this work, the potential of PSN is compared between subgrain populations only and not to effects of other nucleation mechanisms.

A subgrain is considered to be at a constituent particle if one or more of its neighboring map points is a constituent particle. Changes in the number of subgrains at constituent particles per texture component, from the as deformed to the partly recrystallized state, are given in Fig. 6(a). There are more random subgrains than deformation subgrains here, even though there are more of the latter in the overall microstructure [Fig. 5 (a, b)]. A wide range of random subgrains in the deformation zones around large particles is common in cold-rolled Al alloys with such particles [5,26]. This means that a strong PSN effect, without orientation dependent pinning of (sub)grain boundaries, usually results in a weak recrystallization texture. This weak texture is a result of a large amount of randomly oriented grains and only a slight preference of CubeND and P grains [26,27], and certainly not one dominated by P and CubeND as observed in this alloy both here and in
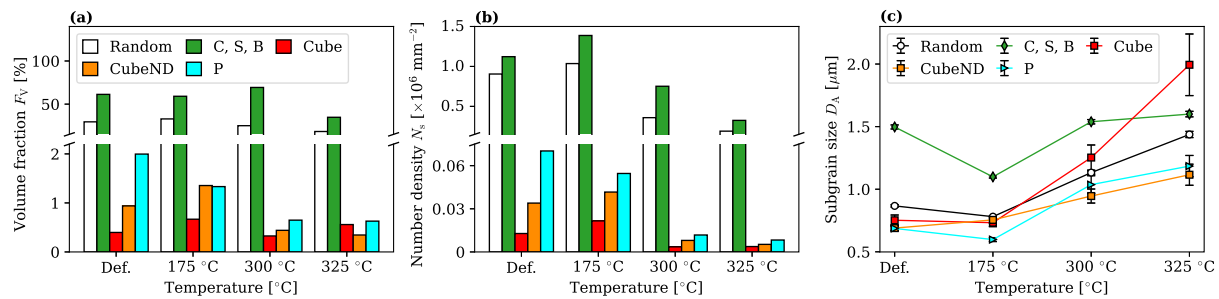
Fig. 5. Subgrain statistics in the cold-rolled and non-isothermally annealed Al–Mn alloy. Values are shown per texture component from the as deformed ('Def.') to the partly recrystallized state. (a) Volume fraction F_V, (b) number of subgrains per area and (c) area weighted subgrain size D_A with 95% confidence intervals. Note the broken vertical axes in (a, b).
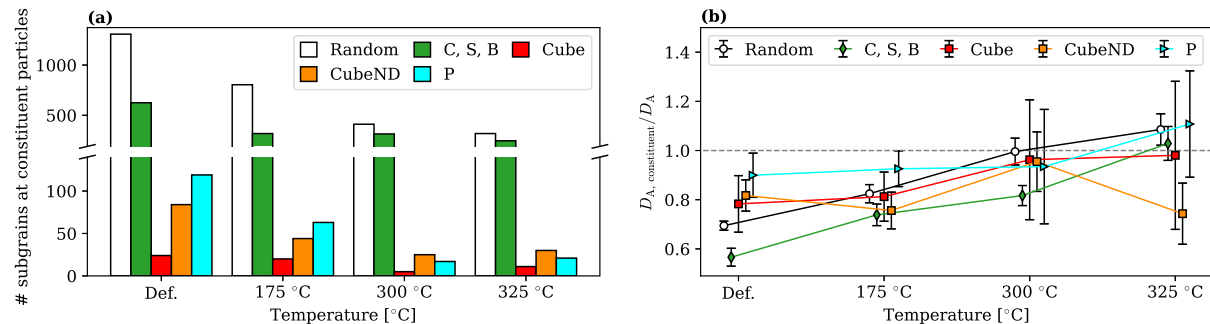

Fig. 6. Subgrains at constituent particles in the cold-rolled and non-isothermally annealed Al–Mn alloy. Values are shown per texture component from the as deformed ('Def.') to the partly recrystallized state. (a) Number of subgrains as a function of texture component. (b) Ratio of sizes $D_{A,\text{constituent}}$ of subgrains at constituent particles over sizes D_A of subgrains elsewhere in the microstructure, with 95% confidence intervals. Note the broken vertical axis in (a). Values in (b) are slightly shifted horizontally to show the individual confidence intervals.

previous works [12]. In the as deformed state, subgrains at constituent particles are smaller than subgrains elsewhere in the microstructure, as evident from the ratio $D_{A,\text{constituent}}/D_A$ presented in Fig. 6(b). This is in accordance with a previous comparison of size distributions of subgrains close to and far away from constituent particles [2]. The 95% confidence intervals for the subgrain size ratios, calculated from error propagation, show relatively high uncertainties for the recrystallization subgrains after recovery. Even so, the ratio increases close to 1 or above for all but CubeND subgrains after partial recrystallization, which means that most subgrains at constituent particles grow faster than subgrains elsewhere. This is a clear indication of a growth advantage of subgrains at constituent particles. This advantage can be understood in terms of both the increased stored energy in the deformation zone around these particles and the reduced dispersoid density and larger dispersoids in this zone.

3.5. Effects of dispersoids on subgrains

A dispersoid is considered to be at a (sub)grain boundary if it is within $0.1\,\mu m$ (the EBSD step size) of it. The cumulative probability of each dispersoid's distance to the closest (sub-)boundary is given in Fig. S6 in the supplementary material. About 60% of dispersoids are located at (sub-)boundaries before recrystallization starts, while only about 40% are after partial recrystallization. If a boundary segment's area is estimated as its length times $2 \times 0.1\,\mu m$, which is an overestimation, boundaries make up about 50% of the total area before recovery, 40% after recovery and 30% after partial recrystallization. Dispersoids formed prior to final annealing in Al alloys are usually observed to be randomly distributed in the deformed microstructure [5,6], and this study finds the same.

In Al–Mn alloys, precipitation during final annealing takes place preferentially at HAGBs rather than low-angle grain boundaries (LAGBs) or dislocations [8,9]. The dependence of the number of dispersoids per sub-boundary length f_L on the boundary misorientation axis and

angle can be investigated with the present data. To express the former, the misorientation axis distributions of all boundary segments and of segments with dispersoids on them are calculated. By subtracting the former distribution from the latter, the relative dispersoid density f_L per misorientation axis is obtained. The density is expressed as the difference in multiples of random density (MRD) away from zero, and visualized in the inverse pole figure of point group $m\bar{3}m$. A misorientation axis having an MRD difference greater (lower) than zero means that the dispersoid density on boundaries with this axis is higher (lower) than on boundaries with other axes. Likewise, the relative dispersoid density per misorientation angle is obtained by subtracting the angle probability histograms of all boundary segments and of segments with dispersoids on them. This density is expressed as a frequency difference in percentage away from zero. Fig. 7 shows the dependence of the relative dispersoid density on sub-boundaries' misorientation axes and angles from the as deformed to the partly recrystallized state. While variations in densities are small, there are some changes with annealing temperature worth noting. In the as deformed state, there are more dispersoids on LAGBs and fewer on HAGBs. With annealing, this difference disappears, until it is reversed in the partly recrystallized state when there are more dispersoids on HAGBs and fewer on LAGBs. Differences in f_L on misorientation axes are seen after recovery and partial recrystallization, when there is a strong concurrent precipitation reaction. After recovery, the relative densities are $f_{L,\langle 111\rangle} > f_{L,\langle 001\rangle} \gg f_{L,\langle 011\rangle}$. After partial recrystallization, the differences in densities have reduced and changed to $f_{L,\langle 011\rangle} > f_{L,\langle 001\rangle} > f_{L,\langle 111\rangle}$. Changes in the dependence of f_L on misorientation axes and angles are caused by both preferential precipitation of new dispersoids and increased pinning of moving boundaries. The observation of an increased f_L on HAGBs with increasing precipitation during final annealing [Figs. 2 (a, b) and 4 (b)] is in line with previous studies [8,9]. The high overall number density n_s of dispersoids provides a high probability of pinning moving boundaries. The initial increased f_L on $\langle 111\rangle$-boundaries after recovery can be understood in terms of these boundaries having an increased
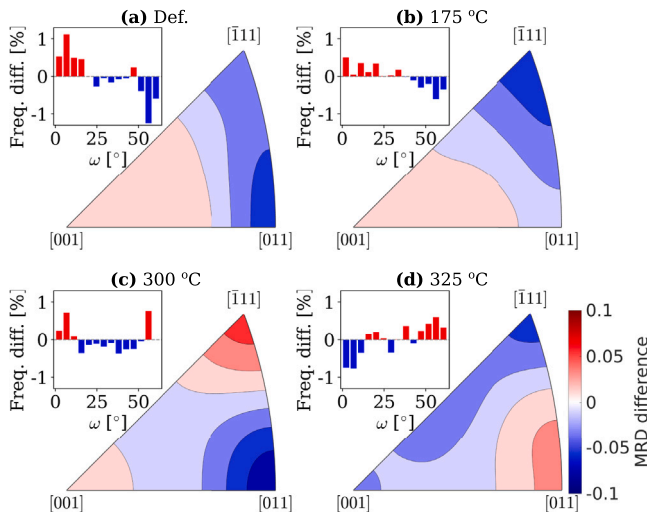
Fig. 7. Dependence of dispersoid densities f_L on misorientation axis and angle, with higher and lower densities above (red) and below (blue) zero, respectively. Relative densities are calculated for the (a) as deformed ('Def') state, (b) before recovery at 175 °C, (c) after recovery at 300 °C and (d) after partial recrystallization at 325 °C of the cold-rolled and non-isothermally annealed Al–Mn alloy. (For interpretation of the references to color in this figure legend, the reader is referred to the web version of this article.)

mobility [28–30] and thus sweeping more dispersoids upon growth [Fig. 5(c)] compared to other boundaries. That $\langle 111 \rangle$-sub-boundaries then have a lower f_L after partial recrystallization seems to indicate that dispersoids precipitated on sub-boundaries during recrystallization favor those of other sub-boundaries than $\langle 111 \rangle$-sub-boundaries.

Variations in the dispersoid density f_L and the average dispersoid size d on sub-boundaries can also be investigated as a function of texture component. In Fig. 8(a) and (b), the dispersoid density and size are shown from the as deformed to the partly recrystallized state. These parameters are comparable for all boundaries before recovery, another indication that dispersoids are distributed quite randomly in the microstructure. Cube and P subgrains grow at a higher rate than other subgrains during recovery [see Fig. 5(c)], which coincides with those subgrains' boundaries having a higher f_L at this condition, with the highest density on Cube sub-boundaries. The observations of increased f_L on $\langle 111 \rangle$-sub-boundaries [Fig. 7(c)] and boundaries of fast growing subgrains are both indications that there is a positive correlation between subgrain growth and an increased sub-boundary dispersoid density during recovery. It also supports the interpretation of the $\langle 111 \rangle$-sub-boundaries being more mobile than other sub-boundaries during recovery. As the dispersoids overall coarsen during recovery [Fig. 4(c)], so do the dispersoids on all sub-boundaries. P sub-boundaries stand out by accommodating much coarser dispersoids [Fig. 8(b)]. After partial recrystallization, the overall number density of dispersoids n_s increases substantially. However, only CubeND sub-boundaries experience a substantial increase in dispersoid density f_L, while other sub-boundaries maintain a similar density as before recrystallization. At this condition, all sub-boundaries except for P sub-boundaries experience a coarsening of dispersoids on them as well, with dispersoids on CubeND sub-boundaries coarsening the most. These results can be combined to give an indication of the Smith–Zener drag on sub-boundaries.

The Smith–Zener drag from randomly distributed dispersoids of average radius $d/2$ on near-planar grain boundaries of average energy γ is given by $P_{SZ} = 3\gamma f_V/d$ [4,5]. However, the fine subgrains and high number density of dispersoids n_s in the as deformed state provide a strong (sub)grain boundary-dispersoid correlation, as about 60% of dispersoids are found at boundaries until the onset of recrystallization while about 40% are at boundaries after partial recrystallization. Furthermore, the interparticle spacing $n_s^{-0.5}$ of dispersoids calculated from
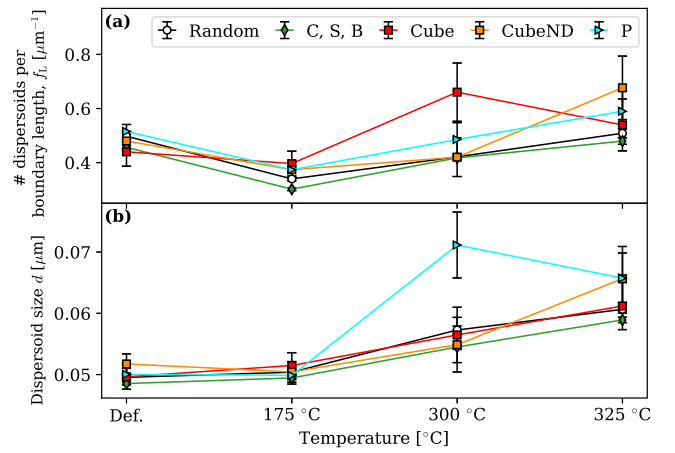

Fig. 8. Dispersoids at sub-boundaries in the cold-rolled and non-isothermally annealed Al–Mn alloy. Values are shown per texture component from the as deformed ('Def.') to the partly recrystallized state, with 95% confidence intervals. (a) Number of dispersoids per boundary length. (b) Dispersoid size per boundary length.
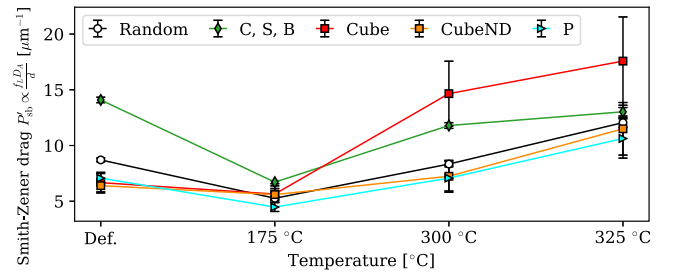

Fig. 9. Modified Smith–Zener drag P'_{sb} at sub-boundaries in the cold-rolled and non-isothermally annealed Al–Mn alloy, calculated from Eq. (1). Values are shown per texture component from the as deformed ('Def.') to the partly recrystallized state, with 95% confidence intervals.

values in Fig. 4(b) is in the order of half the average subgrain size D_A, meaning that the assumption that dispersoids encounter a near-planar boundary is incorrect. For these reasons, a modified expression for P_{SZ} must be used. Hutchinson and Duggan [31] argued that when a large fraction of the particles lie at sub-boundaries, the drag force per unit area of sub-boundary can be written as $P_{sb} = 3\gamma_{sb} f_V/(A_{sb} d^2)$, where A_{sb} is the area of sub-boundary per unit volume and γ_{sb} is the average sub-boundary energy. If the average sub-boundary edge length is L, we can assume that $A_{sb} = 3/L$ [5] to get $P_{sb} = \gamma_{sb} f_V L/d^2$. By expressing the dimensionless average dispersoid volume fraction f_V as $f_L d/2$ per texture component, where f_L is the number of dispersoids per boundary length given in Fig. 8(a), and by approximating L by D_A, we arrive at a modified expression for the Smith–Zener drag at sub-boundaries per texture component:

$$P'_{sb} = \frac{\gamma_{sb} f_L D_A}{2d} \propto \frac{f_L D_A}{d}, \tag{1}$$

where the possible differences in γ_{sb} are neglected. P'_{sb} per texture component is plotted in Fig. 9, with the confidence intervals calculated from error propagation of the confidence intervals of f_L, D_A and d. Prior to recovery, all recrystallization subgrains experience a similar drag from dispersoids. The variations in P'_{sb} in the as deformed state are mostly due to variations in D_A, shown in Fig. 5(c). After recovery, Cube sub-boundaries experience the highest drag, while the drag on P and CubeND sub-boundaries increases only slightly, even though all these subgrains have grown in size. After partial recrystallization, the drag on Cube sub-boundaries remains significantly higher, while the drag on all other sub-boundaries is comparable.

Table 1

Dispersoid density f_L and average dispersoid size d with 95% confidence intervals at the boundaries of 17 recrystallized grains in the partly recrystallized state at 325 °C of the cold-rolled and non-isothermally annealed Al–Mn alloy.

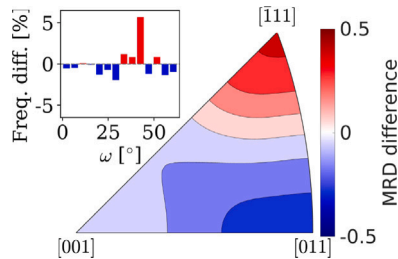| Texture comp.	Random	C, S	Cube	CubeND	P
f_L [μm^{-1}]	0.31 ± 0.04	0.44 ± 0.05	0.98 ± 0.22	0.78 ± 0.12	0.13 ± 0.05
d [μm]	0.066 ± 0.003	0.064 ± 0.002	0.064 ± 0.006	0.056 ± 0.003	0.061 ± 0.004

Fig. 10. Dependence of dispersoid densities f_L on misorientation axis and angle of recrystallized grain boundaries, with higher and lower densities above (red) and below (blue) zero, respectively. Relative densities are calculated for the material after partial recrystallization at 325 °C of the cold-rolled and non-isothermally annealed Al–Mn alloy. (For interpretation of the references to color in this figure legend, the reader is referred to the web version of this article.)

3.6. Effects of dispersoids on recrystallized grains

Huang et al. [12] reported a recrystallized grain size $D = 199.6$ μm after non-isothermal annealing of the present alloy to 325 °C followed by holding at that temperature for 10^5 s. The present experimental approach requires a relatively high BSE image resolution (∼0.026 μm) and may thus not be the best way to acquire correlated datasets of dispersoids and such large recrystallized grains with statistical significance. Nonetheless, there are in total 17 recrystallized grains in the correlated datasets from the partly recrystallized state at 325 °C. All texture components except for B are represented. The density f_L and average size d of dispersoids at the boundaries of these recrystallized grains per texture component are presented in Table 1. The relatively broad 95% confidence intervals of the densities reflect the limited number of recrystallized grains analyzed. However, these results indicate that rapidly growing Cube and CubeND grains experience a higher pinning pressure than rapidly growing P grains during recrystallization, supporting similar observations made by Huang et al. [12]. There is no significant difference in the average dispersoid size on the boundaries.

The variations in relative dispersoid densities on boundaries of recrystallized grains with misorientation axis and angle, as shown in Fig. 7 for sub-boundaries, are shown in Fig. 10. The densities vary much more on recrystallized grain boundaries than on the sub-boundaries. There is a clearly higher density of dispersoids on 35–45°-boundaries and ⟨111⟩-boundaries which is not seen on the sub-boundaries at the same partly recrystallized condition [Fig. 7(d)]. That ⟨111⟩-boundaries of subgrains after recovery and of recrystallized grains after partial recrystallization have higher dispersoid densities than other boundaries are strong indications that ⟨111⟩-boundaries are more mobile and thus sweep more dispersoids during subgrain growth and recrystallization, respectively. Note that the 35–45°-boundaries and ⟨111⟩-boundaries are not necessarily Σ7-boundaries. The boundaries of more recrystallized grains must be incorporated in the analysis to allow such a classification of boundaries into different types.

4. Discussion

It is clear from the presented results that particles affect the nucleation and growth of Cube, CubeND and P (sub)grains differently during recovery and recrystallization. In the following, a brief summary of the nucleation and growth mechanisms of these textures in cold-rolled Al–Mn alloys is given, followed by a discussion of the present results based on a competition between these mechanisms in the presence of concurrent precipitation.

Recrystallization textures in Al alloys are generally characterized by preferential nucleation of subgrains of certain orientations, followed by preferential growth of some of these subgrains to become recrystallized grains [3,5,32]. The main nucleation sites of Cube orientations are band-like structures already present in the as deformed microstructure and retained HAGBs [26,33]. The Cube nuclei have been observed to recover faster than other nuclei, either dynamically during deformation or statically during recovery, thus gaining an often considerable size advantage [34,35]. In addition to these favorable nucleation conditions, Cube grains have a close to 38°⟨111⟩ orientation relationship, or Σ7 in coincident site lattice terminology, to grains of the S orientation, which is, as the C and B orientations, a significant deformation texture component in most cold-rolled Al alloys, and also in the present alloy. Grains with this orientation relationship to neighboring grains have been observed to grow faster than grains with general HAGBs [28,30]. As for the CubeND and P orientations, as mentioned above in Section 3.4, a slight preference for these orientations has been observed among the subgrains growing out of deformation zones around larger particles, i.e. PSN. This preference of CubeND and P nuclei is explained by their close to Σ7-orientation relationships to C grains, which have been observed experimentally [12,26].

There are many reports on the development of strong CubeND and P recrystallization textures in supersaturated Al–Mn alloys after significant concurrent precipitation [9–12,36]. The preference of these textures over the Cube texture is mainly attributed to two mechanisms: (1) an increased suppression of nucleation from Cube-bands and HAGBs by existing and concurrently precipitated dispersoids, effectively promoting the effect of PSN, and (2) an increased growth advantage of the CubeND and P textures due to a reduced solute drag and Smith–Zener pinning effect from dispersoids because, presumably, a larger fraction of their boundaries are of Σ7-type.

The results presented in this work clearly indicate an increased suppression of Cube nuclei. The initial size advantage of Cube subgrains during recovery seen in Fig. 5(c) indicates a faster recovery, which results in an increased Smith–Zener drag P'_{sb} due to the high density of dispersoids precipitated prior to recrystallization (see Fig. 4 (a, b) and e.g. Refs. [10,12]). There are also relatively more and smaller dispersoids in the microstructure away from constituent particles where Cube nucleation sites are typically located. This increased pinning effectively hinders the initial size advantage of Cube subgrains to become significant, and thus the domination of the Cube texture. The importance of the size advantage for the Cube texture was discussed by Vatne et al. in a supersaturated AA3103 alloy [7]. Their alloy had a similar microchemistry to the present alloy, with a strong potential for PSN, due to a considerable amount of large particles, and a significant concurrent precipitation reaction. In contrast to the present recrystallized texture, they observed a texture dominated by Cube, which was explained by the Cube subgrains reaching an overcritical size sooner than PSN subgrains, and thus not experiencing as strong a Smith–Zener drag as the latter subgrains. That an orientation dependent Smith–Zener drag in these similar alloys results in very different recrystallization textures illustrates the delicate balance between nucleation and growth mechanisms during recovery and recrystallization with concurrent precipitation.

The promoted effect of other nucleation mechanisms due to the weakened nucleation of the Cube texture, like PSN, is a strong contributing factor to the increased P and CubeND textures. The P and CubeND textures also have a frequency advantage over Cube in the as deformed state, especially P, as seen in Fig. 5 (a, b). This observation is made possible due to the relatively robust indexing of small subgrains in highly deformed Al-alloys using dictionary indexing [22]. The frequency advantage of P and CubeND among the subgrains in deformation zones around larger particles is even greater [see Fig. 6(a)]. The reduced Smith–Zener pinning potential in the deformation zones due to fewer and larger dispersoids in these zones strengthens this frequency advantage. The P texture has a slight frequency advantage over the CubeND texture [Fig. 5 (a, b)], P subgrains seem to grow faster than CubeND subgrains during recovery [Fig. 5(c)], while P subgrains at constituent particles seem to grow faster than CubeND subgrains during recrystallization [Fig. 6(b)]. Apart from these differences, the present work indicates that effects from PSN and from the modified Smith–Zener drag P'_{sb} vary little for P and CubeND subgrains.

The only substantial difference observed between the P and CubeND textures is the much lower dispersoid density f_L on boundaries of recrystallized P grains compared to that on CubeND grain boundaries in the partly recrystallized state [see Table 1]. The reason for this difference is not clear from the present data. However, such a substantial difference could explain the observed dominance of P compared to the CubeND texture. It is noted that this possible explanation is based on limited statistical evidence of four P and two CubeND recrystallized grains. A natural continuation of the present work is therefore to investigate a larger sample area and hence more of these boundaries in the partly recrystallized state. This would improve the statistics, and might confirm the indication of a lower dispersoid density on boundaries of recrystallized P grains.

We have in this work demonstrated the application of a novel correlated procedure, recently introduced in a related paper by the authors [13], to directly correlate (sub)grains and particles during recovery and recrystallization in an Al–Mn alloy. The methodology combines (sub)grain data from EBSD and particle data from BSE images, enabling a new correlated quantitative analysis of (sub)grains in deformation zones surrounding constituent particles and dispersoids located at (sub)grain boundaries. It is demonstrated that this methodology enables a better understanding of the mechanisms behind the orientation dependent nucleation and growth behavior during recovery and recrystallization in Al–Mn alloys in conditions of strong concurrent precipitation, and in particular the weak Cube texture compared to the stronger P and CubeND textures.

5. Concluding remarks

Multimodal datasets comprising direct spatial correlation of constituent particles and dispersoids with the microstructure in terms of (sub)grains and (sub-)boundaries were analyzed based on BSE imaging and EBSD. The presented results suggest the following causes for the dominating P and CubeND recrystallization textures in a cold-rolled and non-isothermally annealed Al–Mn alloy with concurrent precipitation:

- The often observed size advantage of Cube subgrains is not achieved due to an increased Smith–Zener drag on their boundaries after recovery and partial recrystallization, thus promoting the effect of PSN.
- Dispersoids in deformation zones around large particles are fewer and larger compared to elsewhere in the microstructure, providing a reduced Smith–Zener drag for PSN nuclei.
- The only advantages of the P texture compared to the CubeND texture are a frequency advantage both in deformation zones around large particles and elsewhere in the microstructure, and a slight size advantage due to faster subgrain growth.

- An indication of a much lower dispersoid density on the boundaries of recrystallized P grains compared to those on CubeND and Cube boundaries was observed, although investigations to improve the statistics are required to further substantiate this observation.

Declaration of competing interest

The authors declare that they have no known competing financial interests or personal relationships that could have appeared to influence the work reported in this paper.

Data and code availability

The raw EBSD datasets and BSE images required to reproduce these findings are available from Zenodo at https://doi.org/10.5281/zenodo.7383087 (Ånes et al., 2022) [23] . All softwares used for analysis of the data are freely available, apart from *MTEX* which requires a *MATLAB* license. *Jupyter* notebooks and *MTEX* and *ImageJ* scripts for most data processing steps are available from the following *GitHub* repository: https://github.com/hakonanes/p-texture-al-mn-alloys.

Acknowledgments

Appendix A. Supplementary data

Supplementary material related to this article can be found online at https://doi.org/10.1016/j.actamat.2023.118761.

References

[1] J. Hirsch, T. Al-Samman, Superior light metals by texture engineering: Optimized aluminum and magnesium alloys for automotive applications, Acta Mater. 61 (3) (2013) 818–843, http://dx.doi.org/10.1016/j.actamat.2012.10.044.

[2] F.J. Humphreys, The nucleation of recrystallization at second phase particles in deformed aluminium, Acta Metall. 25 (11) (1977) 1323–1344, http://dx.doi.org/10.1016/0001-6160(77)90109-2.

[3] O. Engler, Nucleation and growth during recrystallisation of aluminium alloys investigated by local texture analysis, Mater. Sci. Technol. 12 (10) (1996) 859–872, http://dx.doi.org/10.1179/026708396790122206.

[4] G.S. Rohrer, "Introduction to grains, phases, and interfaces—an interpretation of microstructure," Trans. AIME, 1948, vol. 175, 15–51, by CS Smith, Metall. Mater. Trans. B 41 (3) (2010) 457–494, http://dx.doi.org/10.1007/s11663-010-9364-6.

[5] F.J. Humphreys, G.S. Rohrer, A.D. Rollett, Recrystallization and Related Annealing Phenomena, third ed., Elsevier, Oxford, 2017, p. 734.

[6] K. Huang, K. Marthinsen, Q. Zhao, R.E. Logé, The double-edge effect of second-phase particles on the recrystallization behaviour and associated mechanical properties of metallic materials, Prog. Mater. Sci. 92 (2018) 284–359, http://dx.doi.org/10.1016/j.pmatsci.2017.10.004.

[7] H. Vatne, O. Engler, E. Nes, Influence of particles on recrystallisation textures and microstructures of aluminium alloy 3103, Mater. Sci. Technol. 13 (2) (1997) 93–102, http://dx.doi.org/10.1179/mst.1997.13.2.93.

[8] M. Somerday, F. Humphreys, Recrystallisation behaviour of supersaturated Al–Mn alloys Part 1–Al–1.3 wt-% Mn, Mater. Sci. Technol. 19 (1) (2003) 20–29, http://dx.doi.org/10.1179/026708303225008626.

[9] S. Tangen, K. Sjølstad, T. Furu, E. Nes, Effect of concurrent precipitation on recrystallization and evolution of the P-texture component in a commercial Al-Mn alloy, Metall. Mater. Trans. A Phys. Metall. Mater. Sci. 41 (11) (2010) 2970–2983, http://dx.doi.org/10.1007/s11661-010-0265-8.

[10] K. Huang, N. Wang, Y. Li, K. Marthinsen, The influence of microchemistry on the softening behaviour of two cold-rolled Al–Mn–Fe–Si alloys, Mater. Sci. Eng. A 601 (2014) 86–96, http://dx.doi.org/10.1016/j.msea.2014.02.037.

[11] Q. Zhao, K. Huang, Y. Li, K. Marthinsen, Orientation preference of recrystallization in supersaturated aluminum alloys influenced by concurrent precipitation, Metall. Mater. Trans. A Phys. Metall. Mater. Sci. 47 (3) (2016) 1378–1388, http://dx.doi.org/10.1007/s11661-015-3314-5.

[12] K. Huang, K. Zhang, K. Marthinsen, R.E. Logé, Controlling grain structure and texture in Al–Mn from the competition between precipitation and recrystallization, Acta Mater. 141 (2017) 360–373, http://dx.doi.org/10.1016/j.actamat.2017.09.032.

[13] H.W. Ånes, A.T.J. van Helvoort, K. Marthinsen, Correlated subgrain and particle analysis of a recovered Al–Mn alloy by directly combining EBSD and backscatter electron imaging, Mater. Charact. (2022) http://dx.doi.org/10.1016/j.matchar.2022.112228.

[14] R. Hielscher, H. Schaeben, A novel pole figure inversion method: Specification of the MTEX algorithm, J. Appl. Crystallogr. 41 (6) (2008) 1024–1037, http://dx.doi.org/10.1107/S0021889808030112.

[15] C.A. Schneider, W.S. Rasband, K.W. Eliceiri, NIH Image to ImageJ: 25 years of image analysis, Nature Methods 9 (7) (2012) 671–675, http://dx.doi.org/10.1038/nmeth.2089.

[16] Y.H. Chen, S.U. Park, D. Wei, G. Newstadt, M.A. Jackson, J.P. Simmons, M. De Graef, A.O. Hero, A dictionary approach to electron backscatter diffraction indexing, Microsc. Microanal. 21 (3) (2015) 739–752, http://dx.doi.org/10.1017/S1431927615000756.

[17] F. de la Peña, T. Ostasevicius, V.T. Fauske, P. Burdet, P. Jokubauskas, M. Nord, M. Sarahan, E. Prestat, D.N. Johnstone, J. Taillon, et al., Electron microscopy (Big and Small) data analysis with the open source software package HyperSpy, Microsc. Microanal. 23 (S1) (2017) 214–215, http://dx.doi.org/10.1017/S1431927617001751.

[18] H.W. Ånes, L. Lervik, O. Natlandsmyr, T. Bergh, Z. Xu, E. Prestat, pyxem/kikuchipy: kikuchipy 0.6.1, 2022, Zenodo. http://dx.doi.org/10.5281/zenodo.6655562.

[19] P.G. Callahan, M. De Graef, Dynamical electron backscatter diffraction patterns. Part I: Pattern simulations, Microsc. Microanal. 19 (2013) 1255–1265, http://dx.doi.org/10.1017/S1431927613001840.

[20] D. Rowenhorst, H.W. Ånes, USNavalResearchLaboratory/PyEBSDIndex: PyEBSDIndex: 0.1.0, 2022.

[21] F. Bachmann, R. Hielscher, H. Schaeben, Grain detection from 2d and 3d EBSD data-Specification of the MTEX algorithm, Ultramicroscopy 111 (12) (2011) 1720–1733, http://dx.doi.org/10.1016/j.ultramic.2011.08.002.

[22] S. Singh, Y. Guo, B. Winiarski, T.L. Burnett, P.J. Withers, M. De Graef, High resolution low kV EBSD of heavily deformed and nanocrystalline Aluminium by dictionary-based indexing, Sci. Rep. 8 (2018) http://dx.doi.org/10.1038/s41598-018-29315-8.

[23] H.W. Ånes, A.T.J. van Helvoort, K. Marthinsen, Electron Backscatter Diffraction Data and Backscatter Electron Images from Four Conditions from a Cold-Rolled and Annealed Al-Mn Alloy, Zenodo, 2022, http://dx.doi.org/10.5281/zenodo.7383087.

[24] P. Furrer, G. Hausch, Recrystallization behaviour of commercial Al-1%Mn alloy, Met. Sci. 13 (3–4) (1979) 155–162, http://dx.doi.org/10.1179/msc.1979.13.3-4.155.

[25] Y. Zhang, D.J. Jensen, Y. Zhang, F. Lin, Z. Zhang, Q. Liu, Three-dimensional investigation of recrystallization nucleation in a particle-containing Al alloy, Scr. Mater. 67 (4) (2012) 320–323, http://dx.doi.org/10.1016/j.scriptamat.2012.05.006.

[26] O. Engler, P. Yang, X.W. Kong, On the formation of recrystallization textures in binary Al-1.3% Mn investigated by means of local texture analysis, Acta Mater. 44 (8) (1996) 3349–3369, http://dx.doi.org/10.1016/1359-6454(95)00416-5.

[27] O. Engler, J. Hirsch, K. Lücke, Texture development in Al-1.8 wt% Cu depending on the precipitation state—II. Recrystallization textures, Acta Metall. Mater. 43 (1) (1995) 121–138, http://dx.doi.org/10.1016/0956-7151(95)90268-6.

[28] K. Lücke, The orientation dependence of grain boundary motion and the formation of recrystallization textures, Canadian Metall. Q. 13 (1) (1974) 261–274, http://dx.doi.org/10.1179/cmq.1974.13.1.261.

[29] C.-C. Yang, A. Rollett, W. Mullins, Measuring relative grain boundary energies and mobilities in an aluminum foil from triple junction geometry, Scr. Mater. 44 (12) (2001) 2735–2740, http://dx.doi.org/10.1016/S1359-6462(01)00960-5.

[30] G. Fan, Y. Zhang, J.H. Driver, D.J. Jensen, Oriented growth during recrystallization revisited in three dimensions, Scr. Mater. 72 (2014) 9–12, http://dx.doi.org/10.1016/j.scriptamat.2013.09.031.

[31] W. Hutchinson, B. Duggan, Influence of precipitation on recrystallization and texture development in an iron-1.2% copper alloy, Met. Sci. 12 (8) (1978) 372–380, http://dx.doi.org/10.1179/msc.1978.12.8.372.

[32] R.D. Doherty, D.A. Hughes, F.J. Humphreys, J.J. Jonas, D.J. Jensen, M.E. Kassner, W.E. King, T.R. McNelley, H.J. McQueen, A.D. Rollett, Current issues in recrystallization: a review, Mater. Sci. Eng. A 238 (2) (1997) 219–274, http://dx.doi.org/10.1016/S0921-5093(97)00424-3.

[33] J. Hjelen, R. Ørsund, E. Nes, On the origin of recrystallization textures in aluminium, Acta Metall. Mater. 39 (7) (1991) 1377–1404, http://dx.doi.org/10.1016/0956-7151(91)90225-P.

[34] S. Bunkholt, E. Nes, K. Marthinsen, Orientation independent and dependent subgrain growth during iso-thermal annealing of high-purity and commercial purity aluminium, Metals 9 (10) (2019) 1032, http://dx.doi.org/10.3390/met9101032.

[35] O. Sukhopar, M. Kuzmina, G. Gottstein, Investigation of the substructure evolution within grains of different orientations during recrystallization in a commercial Al alloy, in: Advanced Materials Research, Vol. 409, Trans Tech Publ, 2012, pp. 71–76, http://dx.doi.org/10.4028/www.scientific.net/AMR.409.71.

[36] K. Huang, Y.J. Li, K. Marthinsen, Microstructural evolution during isothermal annealing of a cold-rolled Al-Mn-Fe-Si alloy with different microchemistry states, in: Materials Science Forum, Vol. 794, Trans Tech Publ, 2014, pp. 1163–1168, http://dx.doi.org/10.4028/www.scientific.net/MSF.794-796.1163.